AGU PUBLICATIONS

JGR

Journal of Geophysical Research: Earth Surface

RESEARCH ARTICLE
10.1002/2017JF004423

Key Points:
- Damage-based brittle creep model simulates long-term evolution of alpine rock slopes from glaciated to postglacial conditions
- Deglaciation and damage-dependent fluid distribution are key controls of shear strain localization and rockslide differentiation
- Insights in temporal evolution of failure mechanisms explain reported Holocene rockslide clusters and support rockslide forecasting

Supporting Information:
- Supporting Information S1

Correspondence to:
F. Agliardi,
federico.agliardi@unimib.it

Citation:
Riva, F., Agliardi, F., Amitrano, D., & Crosta, G. B. (2018). Damage-based time-dependent modeling of paraglacial to postglacial progressive failure of large rock slopes. *Journal of Geophysical Research: Earth Surface*, *123*, 124–141. https://doi.org/10.1002/2017JF004423

Received 10 JUL 2017
Accepted 12 DEC 2017
Accepted article online 20 DEC 2017
Published online 10 JAN 2018

Damage-Based Time-Dependent Modeling of Paraglacial to Postglacial Progressive Failure of Large Rock Slopes

Federico Riva[1], Federico Agliardi[1], David Amitrano[2], and Giovanni B. Crosta[1]

[1]Department of Earth and Environmental Sciences, Università degli Studi di Milano–Bicocca, Milan, Italy, [2]ISTerre, Université Grenoble Alpes, Grenoble, France

Abstract Large alpine rock slopes undergo long-term evolution in paraglacial to postglacial environments. Rock mass weakening and increased permeability associated with the progressive failure of deglaciated slopes promote the development of potentially catastrophic rockslides. We captured the entire life cycle of alpine slopes in one damage-based, time-dependent 2-D model of brittle creep, including deglaciation, damage-dependent fluid occurrence, and rock mass property upscaling. We applied the model to the Spriana rock slope (Central Alps), affected by long-term instability after Last Glacial Maximum and representing an active threat. We simulated the evolution of the slope from glaciated conditions to present day and calibrated the model using site investigation data and available temporal constraints. The model tracks the entire progressive failure path of the slope from deglaciation to rockslide development, without a priori assumptions on shear zone geometry and hydraulic conditions. Complete rockslide differentiation occurs through the transition from dilatant damage to a compacting basal shear zone, accounting for observed hydraulic barrier effects and perched aquifer formation. Our model investigates the mechanical role of deglaciation and damage-controlled fluid distribution in the development of alpine rockslides. The absolute simulated timing of rock slope instability development supports a very long "paraglacial" period of subcritical rock mass damage. After initial damage localization during the Lateglacial, rockslide nucleation initiates soon after the onset of Holocene, whereas full mechanical and hydraulic rockslide differentiation occurs during Mid-Holocene, supporting a key role of long-term damage in the reported occurrence of widespread rockslide clusters of these ages.

1. Introduction

Large rock slope instabilities in alpine (i.e., formerly glaciated) environments span the transition from glacial to postglacial conditions through a period of paraglacial readjustment, when the evolution of deglaciated landscapes is still directly conditioned by the effects of glaciation on topography, hydrology, and vegetation (Ballantyne, 2002; Church & Ryder, 1972). For slope processes, the exact nature and duration of the paraglacial period are still debated, as well as paraglacial controls on rocks slope instabilities (Agliardi et al., 2009; Ballantyne, 2002; Cruden & Hu, 1993).

Glaciation and deglaciation had an extremely important impact in the European Alps, due to the extent of Quaternary glaciations, Last Glacial Maximum (LGM), and later readvances (Ivy-Ochs et al., 2006; Wirsig et al., 2016). Over the long term, glacial erosion shapes valley flanks (Figure 1a) and influences the distribution of gravitational stresses in deepened and enlarged valleys (Crosta et al., 2013; McColl, 2012; Wirsig et al., 2016). Glacier retreat results in slope debuttressing and influences slope stability through several processes, including stress perturbation with respect to a pure gravitational one (Augustinus, 1995), crack damage, loss of rock mass strength, enhanced weathering, and groundwater flow (Ballantyne, 2002; Crosta, 1996; Harbor, 1992; Holm et al., 2004; Savage et al., 1985; Figure 1b).

The interplay between deglaciation rate, glacially conditioned relief (i.e., valley overdeepening/oversteepening), inherited geological structure (Agliardi et al., 2001), rock mass properties (Harbor, 1992), tectonic or locked-in stresses (Leith et al., 2014; Miller & Dunne, 1996; Savage et al., 1985), fluvial incision and static fatigue processes (Eberhardt et al., 2004; Molnar, 2004; Pariseau & Voight, 1979) may result in a variety of slope failure types and timings, including enhanced rockfall activity, sudden catastrophic failures, or slow rock slope deformations (Ballantyne, 2002; Cossart et al., 2008; Deline et al., 2015; McColl, 2012). On the long term, the latter leave major geomorphic signatures in the long and cross profiles of alpine valleys (Brocklehurst & Whipple, 2004; Korup et al., 2010; Sternai et al., 2011) and may eventually stabilize, continue to creep, or evolve to catastrophic collapse after several thousands of years (El Bedoui et al., 2009).

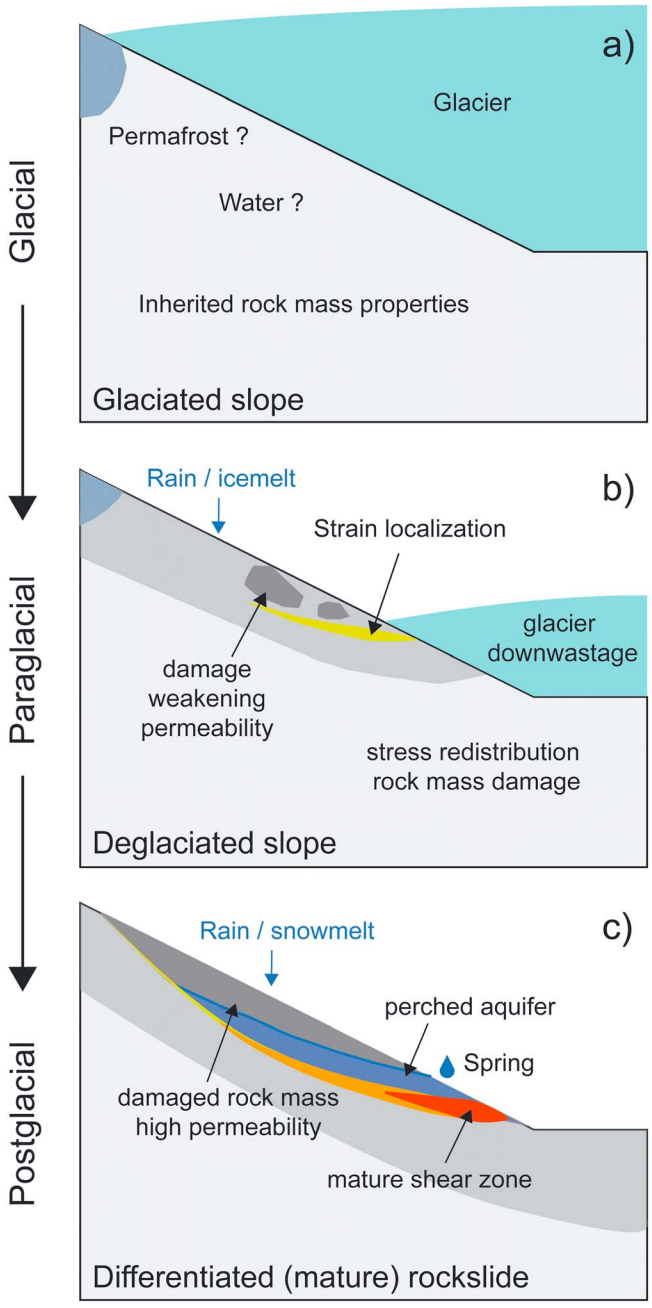

Figure 1. Conceptual glacial to postglacial slope evolution. (a) In glacial conditions rock masses are assumed to be characterized by inherited damage and permeability. (b) In paraglacial conditions progressive brittle damage leads to rock mass weakening and permeability increase. (c) Rockslide differentiation occurs through the development of a mature basal shear zone and a weak, permeable rockslide mass hosting perched aquifers.

During postglacial evolution, external triggers including rainfall and snowmelt can promote or contribute to a range of instabilities reaching up to entire valley flanks, with severe impacts on human lives, activities and infrastructures (Agliardi et al., 2012; Crosta & Agliardi, 2003; Crosta et al., 2014; Dortch et al., 2009; Helmstetter & Garambois, 2010; Zangerl et al., 2010). Large "differentiated" (i.e., mature) rockslides, characterized by well-developed basal shear zones and highly fractured and permeable unstable masses, show the most distinctive sensitivity of displacement patterns to hydrological triggers (Corominas et al., 2005; Crosta et al., 2014; Vallet et al., 2015). Nevertheless, the geomechanical and hydrological legacies of glacial and paraglacial processes and their influence on the postglacial evolution of rock slope instabilities are still poorly known.

Large rock slope failures are commonly delayed with respect to deglaciation, supporting the hypothesis that they undergo progressive failure in subcritical stress conditions (Brideau et al., 2009; Chigira, 1992; Eberhardt et al., 2004). These are mirrored by a commonly observed time-dependent "slope creep" (Emery, 1979), characterized by rather constant, low displacement rates to which seasonal accelerations are often superimposed (Crosta & Agliardi, 2003; Vallet et al., 2015). The latter are usually interpreted as evidence of coupling between hydrological triggers and landslide systems (Crosta et al., 2014; Preisig et al., 2016; Vallet et al., 2015). Although movements progressing to catastrophic collapse may result from rock mass failure without external forcing (i.e., tertiary creep; Rose & Hungr, 2007; Saito & Uezawa, 1961; Voight, 1989; Zavodni & Broadbent, 1978), hydromechanical coupling has been recognized to play an increasingly important role as rockslides attain mature stages of evolution (Crosta et al., 2014).

Modeling the time-dependent behavior of large rock slope instabilities is crucial to predict future displacements and potential catastrophic evolution for risk analysis, early warning, and civil protection purposes (Crosta et al., 2014). In principle, this would require tracking the mechanical and hydrological history of alpine rock slopes to the occurrence of a "mature" rockslide, through a variably long period of transition (Figure 1). In practice, rockslide forecasting mostly relies on analytical, statistical, or numerical models accounting for the hydromechanical landslide response to rainfall or snowmelt (Cappa et al., 2004; Crosta et al., 2014; Guglielmi et al., 2005; Preisig et al., 2016; Vallet et al., 2015; Zangerl et al., 2010), based on a rockslide model derived from geotechnical and geophysical characterization. Nevertheless, the long-term evolution of the geometry, internal structure, strength, and hydrology of alpine rocks slopes is usually unknown and poorly described by models focused on the analysis of onset mechanisms of rock slope failure and their topographic, lithological, structural, and climatic controls (Agliardi et al., 2001; Ambrosi & Crosta, 2006). Attempts to model different stages of long-term alpine rock slope evolution must face several *caveats*, including (a) limitations of rheological approaches to the time-dependent modeling of slope evolution, unless a landslide shear zone is predetermined (De Caro et al., 2016); (b) lack of knowledge regarding progressive evolution of fractures under nearly constant gravitational stress conditions; (c) almost unknown spatial and temporal water distribution in the slope during and after deglaciation (Crosta et al., 2013; McColl, 2012); (d) limited knowledge of the damage-dependent evolution of rock mass permeability on the scale and stress

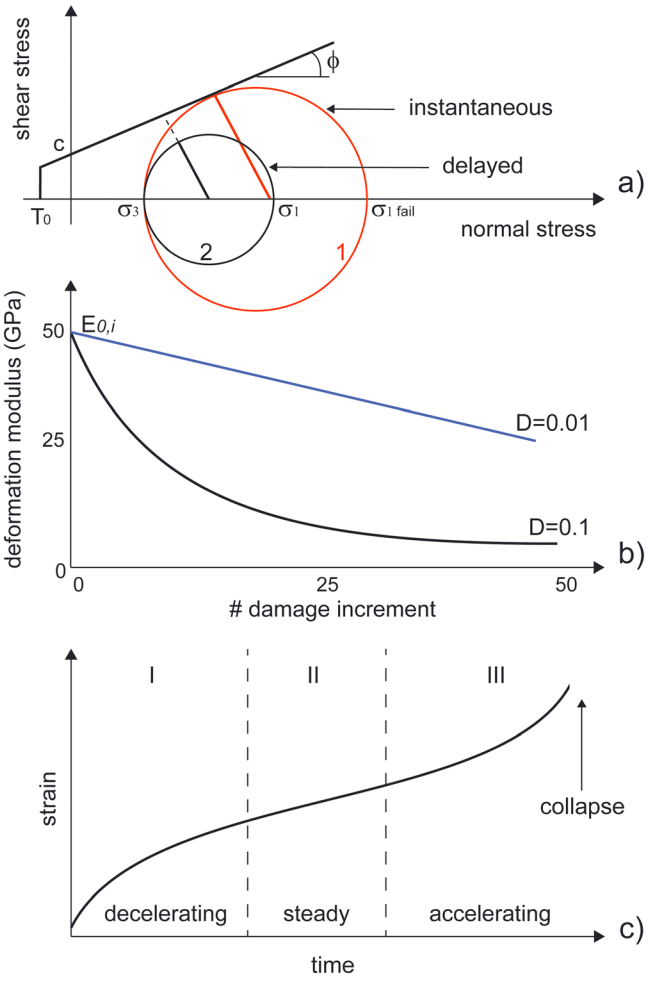

Figure 2. Progressive damage effects leading to macroscopic brittle creep. (a) Instantaneous failure (stress state 1) versus progressive failure occurring in subcritical stress conditions (stress state 2, equation (2)); (b) decrease in deformation modulus corresponding to damage accumulation in a continuum damage mechanics framework (equation (1)). The damage increment parameter *D* regulates the amount of crack damage in each finite element undergoing a rupture event (Amitrano & Helmstetter, 2006); and (c) complete slope creep curve (modified after Saito & Uezawa, 1961).

conditions of rock slopes; and (e) limited understanding of hydromechanical controls on rockslide differentiation, as a major input to the development of rockslide forecasting.

We captured the stages of the alpine rock slope life cycle within one modeling framework, including the effects of time-dependent deglaciation, evolving strength, permeability and water occurrence. We developed our model starting from a damage-based time-dependent approach proposed to simulate laboratory rock deformation experiments (Amitrano & Helmstetter, 2006). We simulated the long-term evolution of the Spriana rock slope (Valmalenco, Italian Central Alps), affected by an active, potentially catastrophic rockslide and characterized by a wealth of geological, site investigation, and monitoring data. We evaluate the potential of damage-based modeling in the understanding of long-term rock slope instability and contribute to a more general discussion of the mechanisms and timing of alpine valley evolution since the LGM.

2. Numerical Model: DaDyn-RS

2.1. Brittle Creep Model

We developed a 2-D finite element model in Matlab™, starting from the "elastic-brittle" modeling approach proposed by Amitrano et al. (1999) and Amitrano and Helmstetter (2006) and applied by Lacroix and Amitrano (2013) to simple slope problems in intact rocks. The model, initially conceived to simulate brittle creep in laboratory rock deformation, combines a time-independent, continuum damage mechanics law (Kachanov, 1986) and a macroscopic time-to-failure law, simulating failure by subcritical crack growth (Atkinson, 1984). Both instantaneous and progressive failure are simulated depending on the local stress state (Figure 2a) using an elastic interaction model, accounting for damage by the progressive degradation of the effective rock deformation modulus at each element (i.e., a macroscopic proxy of crack density; Amitrano & Helmstetter, 2006; Figure 2b). This successfully reproduces both primary and tertiary creep as the damage distribution becomes increasingly localized. Our model is different from the cohesive-brittle-frictional (strain-dependent cohesion reduction and friction mobilization; Martin & Chandler, 1994) or strain softening models (Hajiabdolmajid et al., 2002), previously used to simulate progressive failure in an elastoplastic and time-independent modeling context. The implementation of this formulation at the finite element scale allows us to evaluate the spatial pattern and track the temporal evolution of brittle damage on the slope scale (Figure 2c).

In our model formulation, a "damage event" can occur in a given finite element as follows: (a) instantaneous failure (stress state 1 in Figure 2a), when mobilized shear stress exceeds an instantaneous material damage threshold, represented by the Mohr-Coulomb failure criterion with tensile cutoff according to the observation made by Heap et al. (2009) based on acoustic emission monitoring; or (b) delayed failure, occurring in subcritical stress conditions at a time predicted by the time-to-failure law (Amitrano & Helmstetter, 2006) as a function of the ratio of the locally mobilized differential stress $(\sigma_1 - \sigma_3)_i$ and the differential stress corresponding to instantaneous failure at same confining pressure (Figure 2a). After *n* damage events affecting an element *i*, the effective deformation modulus E_i is decreased depending on an incremental damage parameter *D*, according to equation (1):

$$E_i(n) = (1 - D_i(n))E_{0,i} \quad (1)$$

where $E_{0,i}$ is the initial (elastic) deformation modulus and $D_{i(n)} = 1-(1-D)^n$ is a proxy of crack density accumulated within the element after *n* damage events (Amitrano & Helmstetter, 2006).

The law relating time to failure to the mobilized state of stress has an exponential form:

$$t_{f,i} = T_0 \exp\left[-b\frac{(\sigma_1 - \sigma_3)_i}{(\sigma_1 - \sigma_3)_{f,i}}\right] \quad (2)$$

where $t_{f,i}$ = time to failure for the element i; $(\sigma_1 - \sigma_3)_i$ is the mobilized effective differential stress, and $(\sigma_1 - \sigma_3)_{f,i}$ is the differential stress corresponding to instantaneous failure at same confining pressure; T_0 and b are the empirical constants of the exponential time-to-failure law (Amitrano & Helmstetter, 2006, and references therein).

The decay of deformation modulus in an element undergoing damage leads to stress redistribution around the element, possibly resulting in an "avalanche" of instantaneous failures in surrounding elements at the same time. When instantaneous failure does not occur after stress redistribution, the local time to failure is updated for each element at every model step, and delayed failure occurs in the model element characterized by the shortest time to failure. Model-scale macroscopic features, including damage and strain localization, rupture event statistics, and the full spectrum of creep behavior, from primary to tertiary (accelerating) stages (Figure 2c), are simulated by the model as emerging properties by the elastic interaction between finite elements with heterogeneous properties (Amitrano & Helmstetter, 2006). In particular, increasingly interconnecting damaged elements lead to the development of macroscopic shear zones and to displacement rate increase until accelerated (tertiary) creep occurs.

Amitrano and Helmstetter (2006) developed their original model (and investigated its parameters) to reproduce laboratory observations on dry, intact rock. On the other hand, large rock slopes frequently exceed 1,000 m in local relief and can be affected by rock slope instabilities up to billions of cubic meters in volume (Agliardi et al., 2013; Crosta et al., 2013). This requires upscaling material properties in order to account for the strength, deformability, and permeability of fractured rock masses (Hoek & Brown, 1980; Rutqvist & Stephansson, 2003). Moreover, alpine slopes undergo time-varying deglaciation and the effects of changing groundwater regimes. In order to deal with large, real rock slopes in fractured rock mass we developed new model components in a Matlab™ modeling environment.

2.2. Rock Mass Property Upscaling

To account for fractured rock mass behavior, we upscaled material properties according to the Hoek-Brown empirical approach (Hoek & Brown, 1980; Hoek et al., 2002). This relies on the observation that rock strength decreases with increasing "sample" size, from intact rock (containing microcracks and textural defects) to rock mass (made of rock blocks and macrocracks/discontinuities). Intact rock properties measured in laboratory tests are scaled to field conditions by the Geological Strength Index (GSI, ranging 5–95; Hoek et al., 2002; Hoek et al., 1995). This empirical parameter describes rock mass structure and alteration, easily quantified in both outcrops (Marinos & Hoek, 2000) and borehole data (Agliardi et al., 2016). The use of GSI allows the estimation of the tensile strength and the equivalent Mohr-Coulomb cohesion and friction coefficient of rock masses, for use within DaDyn-RS. The GSI also allows us to derive initial values of rock mass deformation modulus E_0 at each element i, using the empirical relation by Hoek and Diederichs (2006) for the undisturbed case:

$$E_{0,i} = E_{\text{lab}}\left(0.02 + \frac{1}{1 + e^{\left(\frac{(60 - GSI_i)}{11}\right)}}\right) \quad (3)$$

where $E_{0,i}$ is the initial rock mass deformation modulus in the element i, and E_{lab} is the Young modulus of intact rock (Hoek et al., 2002). Assuming a normal distribution for real populations of GSI values, we also use equation (3) to generate corresponding distributions of E_0 to be introduced in initial model setup to account for material heterogeneity.

While the upscaling rules above can be applied to instantaneous strength and deformability properties of rock masses, we have no strong physical arguments allowing a direct upscaling of time dependent properties, especially b. Nevertheless, sensitivity analyses performed by Riva et al. (2016) and Riva (2017) outlined very limited scale effects on these properties, which at this stage can be considered scale independent (see also Figure S1 in the supporting information).

2.3. Time-Dependent Deglaciation

To simulate the effects of deglaciation, we adapted the approach of Lacroix and Amitrano (2013) to complex slope profiles. In our model, ice load is accounted for by applying separated horizontal and

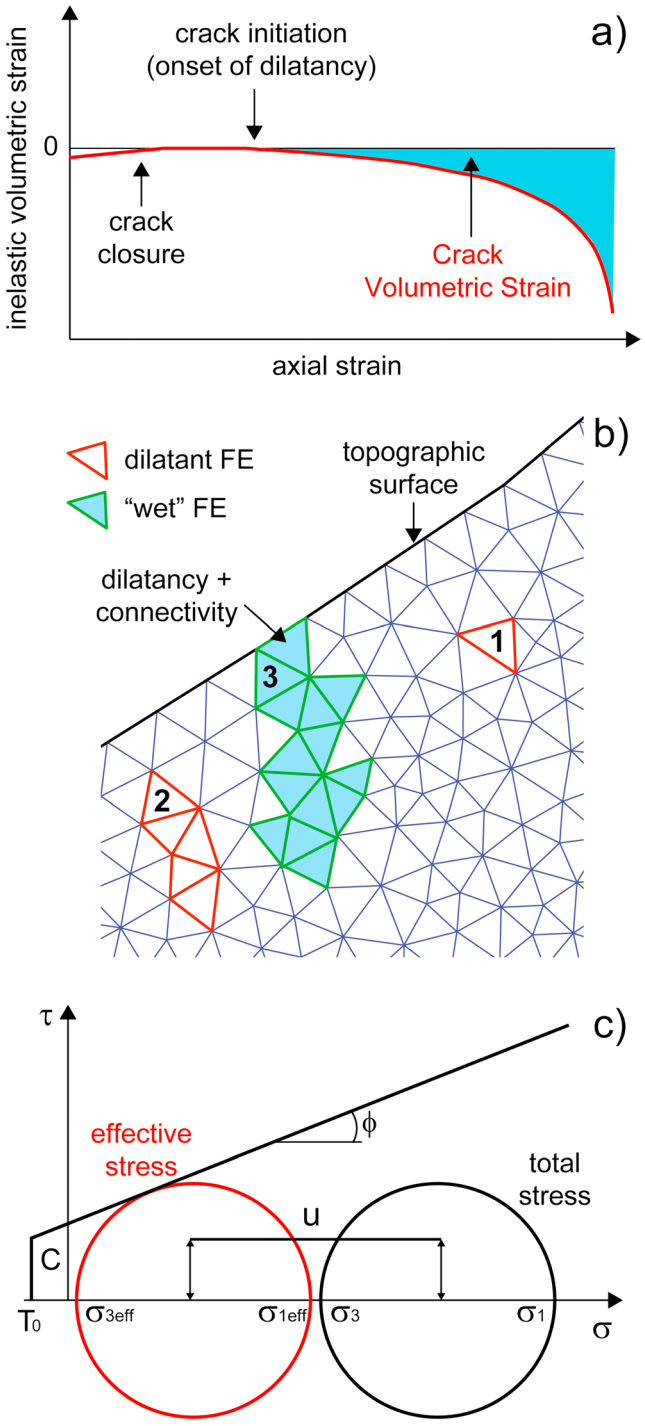

Figure 3. Damage-dependent fluid occurrence in DaDyn-RS. (a) Conceptual volumetric versus axial strain curve for compression tests on intact rocks (after Martin & Chandler, 1994), (b) permeable element cluster definition depending on damage, dilatancy, and connectivity. Water pressure is applied only in Cluster 3 (dilatant and connected with surface) assuming a water infilling percentage; and (c) effective versus total stresses in "wet" element clusters.

vertical ice loads components in order to obtain an overall, transient "hydrostatic" ice load on finite element mesh nodes at slope surface. The timing of deglaciation is updated independently on the model creep time (governed by equation (2)) and calibrated on available absolute or relative chronological constraints (Bini et al., 2009; Wirsig et al., 2016). Two parameters control the timing of deglaciation, namely, the starting time of deglaciation (t_{d0}) and the deglaciation duration (T_d). Under the assumption of constant deglaciation rate, T_d is discretized in time intervals ΔT_d, each corresponding to 1 m of ice removal. Ice load is applied as an external force depending on current ice thickness. The model refreshes stresses at every ΔT_d, or less in case one or more damage events are predicted by the time-to-failure law during an ice removal stage. This condition allows the model to better simulate deglaciation effects on progressive damage, especially for fast deglaciation rates, when due to abrupt stress release many elements can fail simultaneously or in a short time span.

2.4. Damage-Dependent Fluid Occurrence

Including the effects of hydromechanical coupling in the long-term modeling of large rock slopes is a necessary yet extremely difficult task. This is due to the almost complete lack of knowledge of slope hydrology and hydraulic boundary conditions in deglaciating settings (Figure 1), including the recharge contribution of melting glaciers, the role of permafrost on the availability and mobility of liquid water in slopes, and the geometry and extent of groundwater below the ice cover (Crosta et al., 2013; McColl, 2012). In addition, while the influence of crack damage on the permeability of rocks has been studied in rock mechanics laboratory and underground field experiments (Fortin et al., 2011; Rutqvist, 2015; Zoback & Byerlee, 1975), the mechanisms and timing of development of rock mass permeability between deglaciation and complete rockslide development (Preisig et al., 2015) are not well known.

Therefore, we need a simplified yet physically based model of water occurrence in the slope during its evolution. To this end, we link water occurrence to the rock mass dilatancy due to progressive brittle damage (Fortin et al., 2011; Martin & Chandler, 1994) following laboratory experiences on damage-dependent rock permeability (Rutqvist, 2015; Zoback & Byerlee, 1975). In our model, fluids can occur in a given finite element if three conditions are met, namely, damage, dilatancy, and connectivity (Figure 3). First, the element needs to have undergone at least one damage event to develop new cracks at the element scale. Depending on the stress path and deformation history, at a given model stage an element can be characterized by net dilatancy (i.e., volume increase) or contraction (i.e., volume decrease). Dilatancy is an established measure of crack growth and increased rock permeability (Eberhardt et al., 1999; Martin & Chandler, 1994; Figure 3a), and we assume that this applies also on the fractured rock mass scale. Fluids can occur in dilatant slope sectors, which are identified in our model by computing the crack volumetric strain (CVS, i.e., accumulated inelastic volumetric strain; Martin & Chandler, 1994) as a proxy of dilatancy. Following Katz and Reches (2004), at each element at every model step, we calculate the CVS_i as the difference between total

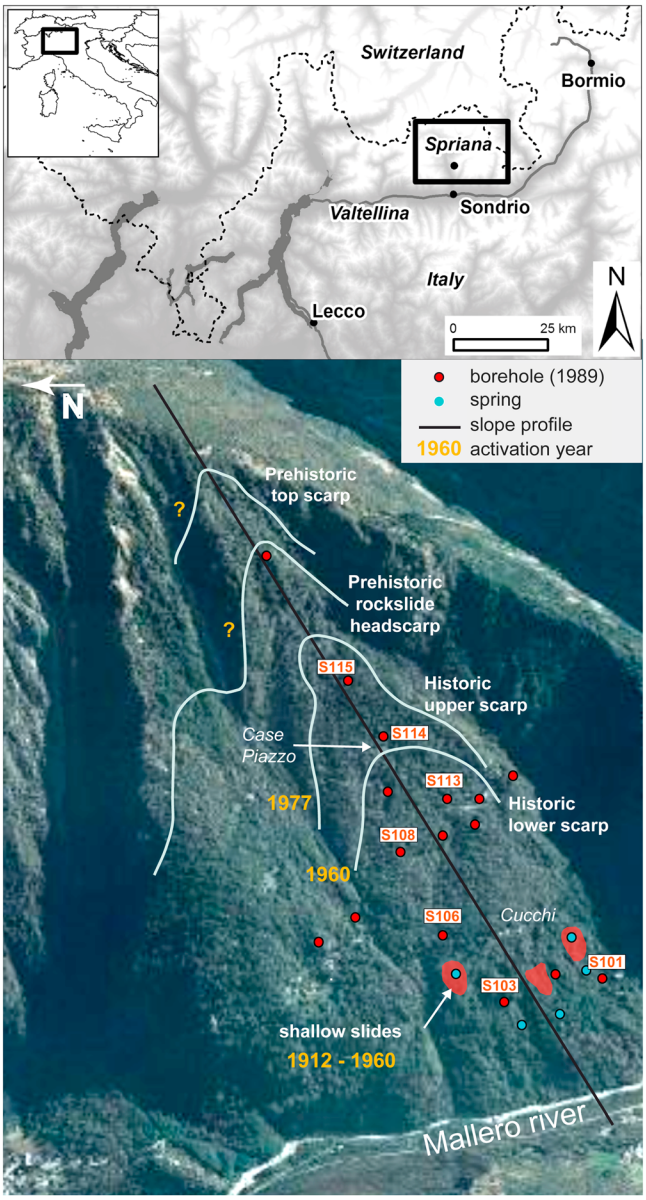

Figure 4. Spriana rockslide location, main morphostructural features and evolutionary stages. Boreholes (1989 site investigation campaign) were used to characterize rockslide structure and damage distributions (Figures 5 and 6).

volumetric strain $(\varepsilon_V)_i$, and the elastic volumetric strain component $(\varepsilon_V)_{E,i}$, the latter depending on initial (undamaged) values of deformation modulus ($E_{0,i}$):

$$\begin{aligned} \mathrm{CVS}_i &= (\varepsilon_V)_i - (\varepsilon_V)_{E,i} \\ (\varepsilon_V)_i &= \varepsilon_{1,i} + \varepsilon_{2,i} \\ (\varepsilon_V)_{E,i} &= (\sigma_{1,i} - \sigma_{3,i})(1 - 2\nu)/E_{0,i} \end{aligned} \tag{4}$$

where ε_1 and ε_2 are the principal strains (positive values denote shortening). Fluids can occur in elements with cumulated CVS < 0, corresponding to net dilatancy. In addition, we assume that fluids enter the slope by percolation from the topographic surface. This requires that dilatant elements are connected each other and to the surface. In our model, elements satisfying previous conditions are checked and grouped in "permeable element clusters," using a hierarchical clustering algorithm (Figure 3b). Clusters of interconnected elements not satisfying the condition of surface connectivity are excluded from the fluid pressure calculation (Clusters 1 and 3 in Figure 3b). Assuming that static water percolates into "permeable element clusters" results in locally hydrostatic conditions (i.e., no flow at this stage of model development). This allows avoiding strong assumptions on hydraulic boundary conditions, which are often unknown over long time periods during glaciation and deglaciation. Fluid pressure is applied to each element in the cluster by imposing a specified degree of cluster filling (w), indirectly accounting for partial drainage effects and ranging from 0 (empty cluster) to 1 (completely filled cluster). Based on fluid pressure calculated at each wet element (u_i), effective stresses (σ'_i) are computed as (Figure 3c):

$$\sigma'_i = \sigma_i - u_i \tag{5}$$

Changes in effective stress distribution can result in both instantaneous failures and an update of the time to failure in subcritically stressed elements (Figure 2c). Thus, damage-dependent fluid occurrence will affect further damage, dilatancy, and water distribution, resulting in a simplified fluid-to-solid hydromechanical coupling cycle (Rutqvist & Stephansson, 2003).

3. Long-Term Modeling of a Real Rock Slope

3.1. The Spriana Rockslide

The Spriana rock slope is located on the left flank of lower Val Malenco (Valtellina, Italian Central Alps) and range in elevation between 550 and 1,800 m above sea level (asl) with a mean slope of 37°. The slope was carved by glacial and fluvial erosion into granodioritic gneiss (Monte Canale unit) characterized by low intact rock porosity (<1.5%) and a complex folded fabric (Agliardi et al., 2014, 2017; Trommsdorf et al., 2005). The slope was completely glaciated during the LGM, when the Malenco glacier reached a maximum local thickness of 800 m and covered the entire slope (Bini et al., 2009). There is no evidence of later significant glacier readvance in this valley sector, which shows evidence of deep incision by the Mallero River.

First documented slope instabilities date back to the late 19th century, when shallow landslides repeatedly occurred in the middle to lower slope sector until 1960, when a period of intense and prolonged rainfall resulted in a global retrogressive activation of rock slope instability. In this period, movements occurred along the rockslide lower scarp (top elevation: 1,160 m asl), leading to the evacuation of the Cucchi village (Figure 4). During 1977–1978 rockslide activity extended upslope through the reactivation of a scarp reaching 1,400 m asl (upper scarp), causing the evacuation of Case Piazzo village. Extensive geotechnical investigations carried out in 1978 and 1989 (Belloni & Gandolfo, 1997) included topographic, geological, and

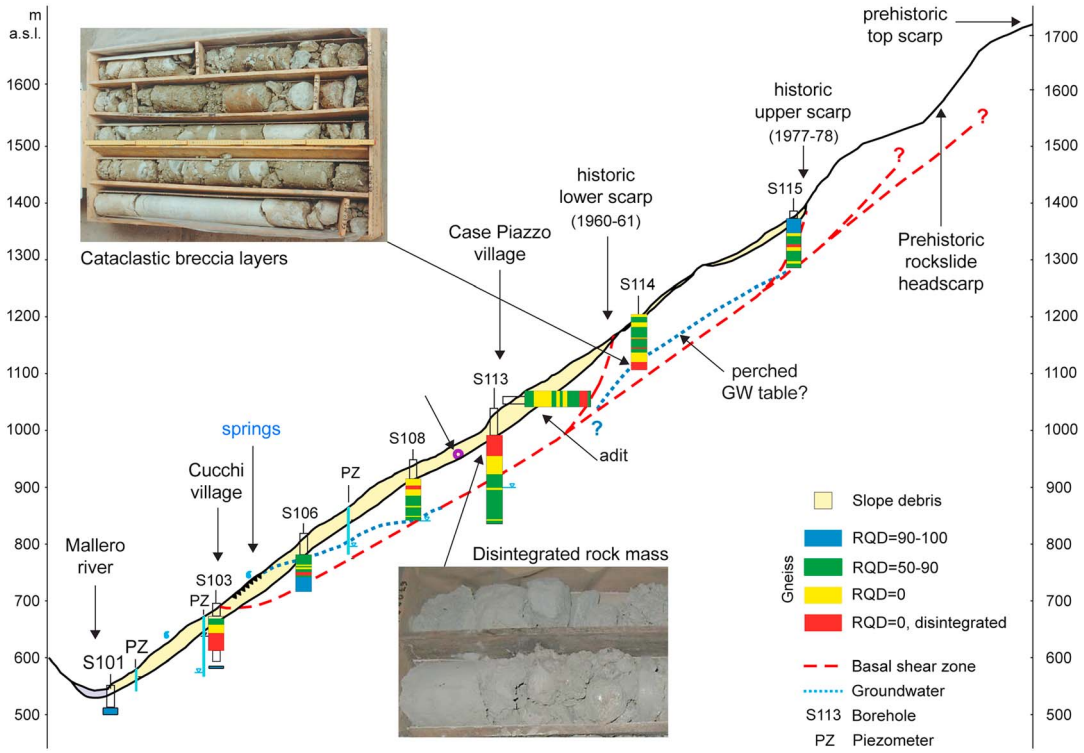

Figure 5. Interpretative model of the Spriana rockslide from field, site investigation, and monitoring data (modified after Agliardi & Crosta, 2014). Example borehole evidence of distributed and localized brittle damage are reported.

geophysical surveys, 20 full-core boreholes and a 140 m long horizontal adit at 1,040 m asl, aimed at the direct investigation of the inferred rockslide basal shear zone. Monitoring activities started with extensive measurements of surface displacement (topographic benchmarks and wire extensometers), subsurface deformation (borehole inclinometers and extensometers), and hydrological variables (meteostations, standpipe, and multipoint piezometers). The network was progressively upgraded, automated, and supported by spaceborne observations by satellite In-SAR monitoring, allowing to review and update (Agliardi & Crosta, 2014) the geological and geotechnical model of the slope (Figure 5).

The active rockslide affects the slope between 700 m and 1,400 m asl over an area of about 0.5 km^2 and involves an estimated 50 Mm^3 of fractured rock mass and debris suspended on the valley floor. Site investigation data suggest that compound sliding (mixed translational/rotational) occurs along a basal shear zone up to 130 m deep in the middle sector, although secondary shear zones occur in the main rockslide body. Three main scarps emerge from the basal shear zone (Figure 5), namely, the lower scarp (top at 1,160 m asl, major activity in 1960), the upper scarp (top: 1,400 m asl, major activity in 1977–1978) and a "prehistoric" rockslide headscarp (top: 1,600 m asl). Despite the lack of documented information, the latter has a sharp geomorphological signature, with a vertical downthrow of about 80 m (Agliardi & Crosta, 2014) and can be traced to the N outside the rockslide, suggesting that a wider area was affected by post-LGM displacements. Further evidence of prehistoric rock slope instability also occurs upslope the Spriana rockslide above 1700 m asl, with a subdued sector (top scarp) with total downthrow exceeding 100 m.

Displacement monitoring carried out since 1978 with topographic, geotechnical, and PS-InSAR measurements (1992–2007, reported in Agliardi & Crosta, 2014) shows continuing rockslide activity. This is characterized by long-term, steady state slope creep, occurring at rates of 0.5–3 cm/a. Sudden or prolonged episodes of displacement rate increase (average up to >20 cm/a) are superimposed on this long-term trend (Agliardi & Crosta, 2014). Borehole records and piezometric data suggest that a perched water table is present into the rockslide mass and likely above the basal shear zone (Belloni & Gandolfo, 1997). The water table is deeper in the upper slope sector and progressively thicker and shallower moving downslope near the Cucchi village, where persistent spring lines were observed (Figures 4 and 5). Recharge of the perched aquifer systems is considered responsible of rockslide acceleration periods. Through the analysis of rainfall, groundwater, and

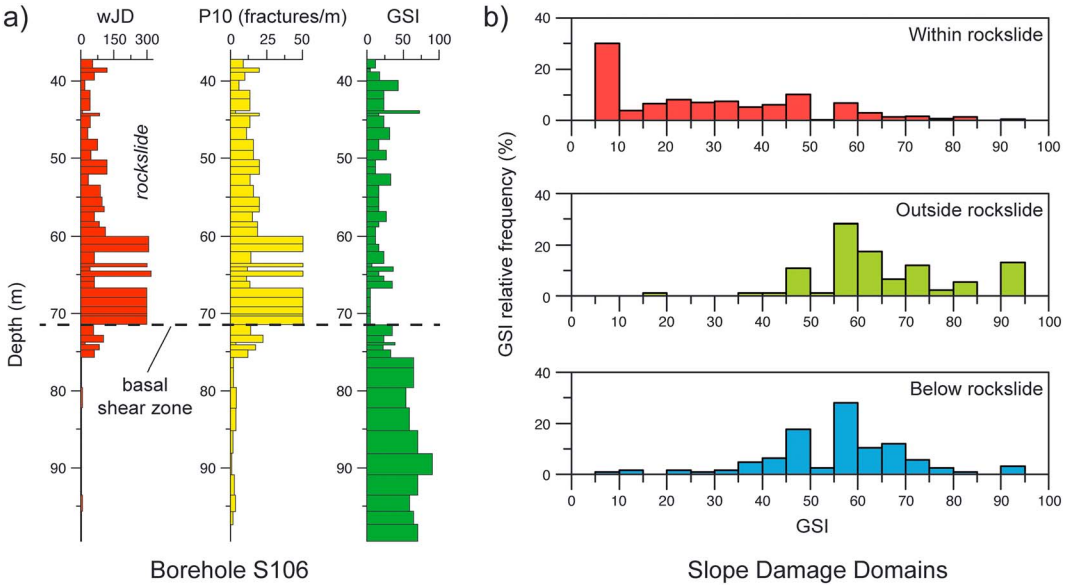

Figure 6. Experimental definition and characterization of slope "damage domains." (a) Example of quantitative geomechanical core logging for individual borehole records (location of S106 in Figure 5); (b) statistical distributions of GSI in different slope domains, providing input and calibration data for modeling. See text for details.

displacement data, Agliardi and Crosta (2014) suggested that major (longer and faster) acceleration periods occur when the water table rise exceeds threshold values (3 m in the middle slope sector).

3.2. Characterization of Slope "Damage Domains"

In order to gather slope material properties for DaDyn-RS model setup and calibration, we performed a complete reexamination of available geomechanical core logging from 17 different boreholes located inside and outside the rockslide (Figures 4 and 5). Detailed geomechanical logging of high-quality drill cores was carried out on 882 core runs for a total core length of 1,048 m. We reclassified the original descriptions of individual discontinuities (discontinuity type, shape, roughness, weathering, dip angle, aperture, and filling material) and logged fracture intensity for each core run. We processed the data set to obtain different quantitative descriptors of fracture intensity and rock mass quality, including the Weighted Joint Density (Palmstrom, 2005), the linear fracture intensity, P_{10} (Dershowitz & Herda, 1992), and the Geological Strength Index, GSI (Agliardi et al., 2016; Hoek et al., 1995) for each core run (Figure 6a).

Reclassified core logs allow us to identify slope domains (within, below, and outside the Spriana rockslide) characterized by contrasting rock mass structure and brittle damage evidence. Rock volumes within the rockslide mass are characterized by a chaotic structure, including: disrupted rock mass volumes (GSI $<$ 20–25) affected by distributed damage (Figure 5); fractured rock masses with evidence of strain localization into shear zones outlined by cataclastic breccia layers of variable thickness (tens of centimeters up to meters); and isolated remnants of relatively undisturbed rock mass. Below the rockslide basal shear zone, the rock mass appears less damaged but still fractured and with episodic occurrence of thin cataclastic layers. Outside the rockslide, boreholes encountered less disturbed rock masses of average quality, affected by scattered submetric layers of intensely fractured rock.

A statistical analysis of GSI populations sampled in the different "damage domains" provided distinct measurable signatures of rock mass damage (Figure 6b). GSI values in the "below" and "outside" domains can be fitted by normal probability distributions, typical of rock mass structures affected by different degrees of damage. The "below" domain is characterized by an average GSI = 55 (standard deviation: 14), whereas the "outside" domain has an average GSI of 65 (standard deviation: 15) but higher frequency of values of GSI $>$ 70. These values provide a figure of rock mass damage inherited from tectonic, glacial, fluvial, and gravitational processes affecting the slope prior to initial rockslide displacement. In the "within" domain, severe damage related to rockslide processes led to the complete loss of rock mass structure (Figure 6b). For DaDyn-RS model setup, we used "outside" rock mass properties (GSI $>$ 70) as initial properties, whereas

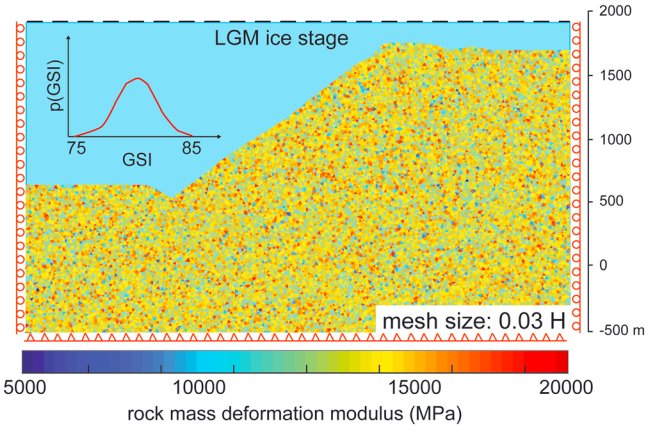

Figure 7. DaDyn-RS model setup for the Spriana case study. The statistical distribution of initial values of rock mass deformation modulus is derived from GSI values (Figure 6) according to the approach proposed by Hoek and Diederichs (2006). H is the maximum elevation difference of the model domain. See text for details.

the domains "within" and "below" the rockslide provided reference strength and damage patterns for the validation of final model states.

3.3. Model Setup and Calibration

Numerical models were set up by discretizing the 2-D slope domain (restored to prefailure conditions based on geomorphological reconstruction) with a mesh of 14,000 three-noded triangular finite elements (Figure 7) with maximum edge size of 35 m (corresponding to 3% of the slope vertical size). This mesh size was selected based on a preliminary sensitivity analysis (Riva, 2017; see also Figure S2 in the supporting information) to optimize model run time (about 25 h on a 64 bit 3.07 GHz Intel® Xeon® CPU with 8 GB RAM). External mesh nodes along the bottom boundary were fixed in both the horizontal and vertical directions, whereas nodes on the lateral boundaries were left free to move vertically.

We parametrized our model starting from the sensitivity analyses for strength, damage, and time-dependent parameters performed by Amitrano and Helmstetter (2006) (laboratory scale and intact dry rocks), Lacroix and Amitrano (2013) (slope scale and intact dry rocks), and Riva (2017) (slope scale and rock masses with variable permeable element cluster filling). In particular, there is no theoretical argument on possible scale dependence of b and D. However, simulation tests carried out by Riva et al. (2016) and Riva (2017) suggest that this dependence is negligible, since the typical geometries, mechanisms of damage patterns of real large rock slopes are reproduced by DaDyn-RS for b and D values in the same order of magnitude of those obtained for intact rock in laboratory tests (here $b = 30$ and $D = 0.1$). To test the influence of water pressures on model response, different simulation runs were performed in both "dry" and "wet" conditions, by imposing values of permeable cluster filling (w) of 0 (i.e., "dry" conditions) and 0.35, respectively.

Initial values of rock mass strength and deformability properties were derived by the analysis of site investigation for the "outside" damage domain (section 3.2), and GSI values of 80 ± 5 were selected to describe initial model conditions. According to the Hoek-Brown approach, the GSI was used to upscale the intact gneiss properties (Agliardi et al., 2014) and derive rock mass tensile, cohesive, and frictional strength, as well as the average value and heterogeneity of the initial deformation modulus E_0 (section 2.2). The Poisson ratio was imposed equal to $\nu = 0.45$, based on the results of sensitivity analyses with DaDyn (Lacroix & Amitrano, 2013; Riva, 2017) and consistent with reported observations of high Poisson's ratios of jointed rock masses at shallow crustal levels (Barton, 2007; Gercek, 2007).

Initial stress (see also Figure S3 in the supporting information) was initialized in the model by applying gravity in each node and external ice load to the slope profile, corresponding to the LGM ice stage (1,950 m asl; Figure 7). Then, the long-term slope evolution was simulated since the LGM through deglaciation (occurred between 21 and 19 ka B.P. depending on the location; Clark et al., 2009; Wirsig et al., 2016, and references therein), Lateglacial and Holocene until present day. The LGM ice stage, the starting time of deglaciation

Table 1
Summary of Calibrated Numerical Model Parameters for the Spriana Rock Slope

Parameter	Symbol	Unit	Average value
Unit weight	γ	kN/m^3	27
Young modulus (intact rock)	E	MPa	22,700
Tensile strength (rock mass)	T	MPa	3.5
Cohesion (rock mass)	C	MPa	7
Coefficient of internal friction (rock mass)	μ	-	1.1
Poisson ratio (rock mass)	ν	-	0.45
Damage increment parameter	D	-	0.10
Time-to-failure law parameter	b	-	30
Permeable cluster water filling	w	-	0.35

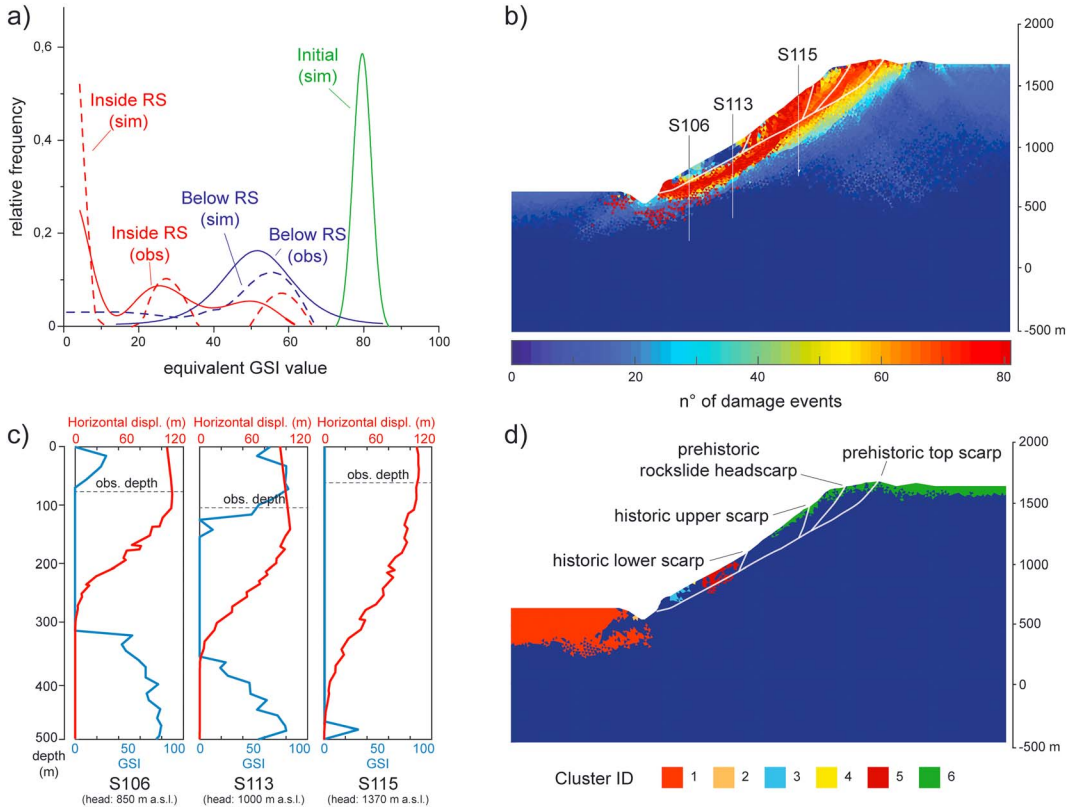

Figure 8. Final state of the calibrated numerical model. (a) Observed versus simulated frequency distributions of GSI values (simulated values are back calculated from distributions of simulated effective deformation moduli, E_i); (b) simulated damage pattern, compared to observed rockslide features (white lines); (c) logs of simulated GSI values recomputed from simulated E_i by equation (3) (i.e., virtual borehole logs) and horizontal displacement (i.e., virtual inclinometers) along vertical lines corresponding to boreholes; and (d) permeable element cluster distribution in the final state, outlining the occurrence of perched aquifers in the differentiated rockslide body.

(t_{d0} = 1 ka after simulation start), and the deglaciation duration (T_d, set to 800 a) were constrained using the most updated available paleo-environmental and chronological data (Bini et al., 2009; Ivy-Ochs et al., 2006, 2008; Wirsig et al., 2016). The simulation stopped when the vertical displacement of the observed prehistoric rockslide headscarp reached 80 m as observed in the field (Figures 4 and 5).

Model parameters were calibrated (Table 1) by optimizing the match of (1) statistical distributions of observed and simulated values of the GSI, back calculated from distributions of effective deformation moduli in slope sectors corresponding to different "damage domains" (Figure 8a); (2) model and field evidence of rockslide geometry (size, depth, toe, and crest locations; Figure 8b), damage patterns (localized versus distributed; Figures 8b and 8c), and displacements (Figures 8c, 9b, and 9c); and (3) simulated temporal evolution versus field or literature constraints (e.g., total model lifetime versus deglaciation time; displacement-time curve). For the Spriana case study, calibrated values of tensile and cohesive strength of 3.5 MPa and 7 MPa, respectively, are in the range of values between those of intact rock (Agliardi et al., 2014) and rock mass. This reflects the importance to account for the effects of rock bridges (i.e., nonpersistent fractures) when simulating the progressive failure of rock slopes (Eberhardt et al., 1999; Einstein et al., 1983). Rockslide depth, kinematics, and degree of damage localization were properly reproduced by imposing a degree of filling of permeable element clusters equal to 0.35.

4. Results and Discussion

4.1. Rockslide Mechanisms

Calibrated model results accounting for upscaled material properties (Figure 8a), time-dependent deglaciation, and damage-dependent water pressure distributions provide a satisfactory account of the observed

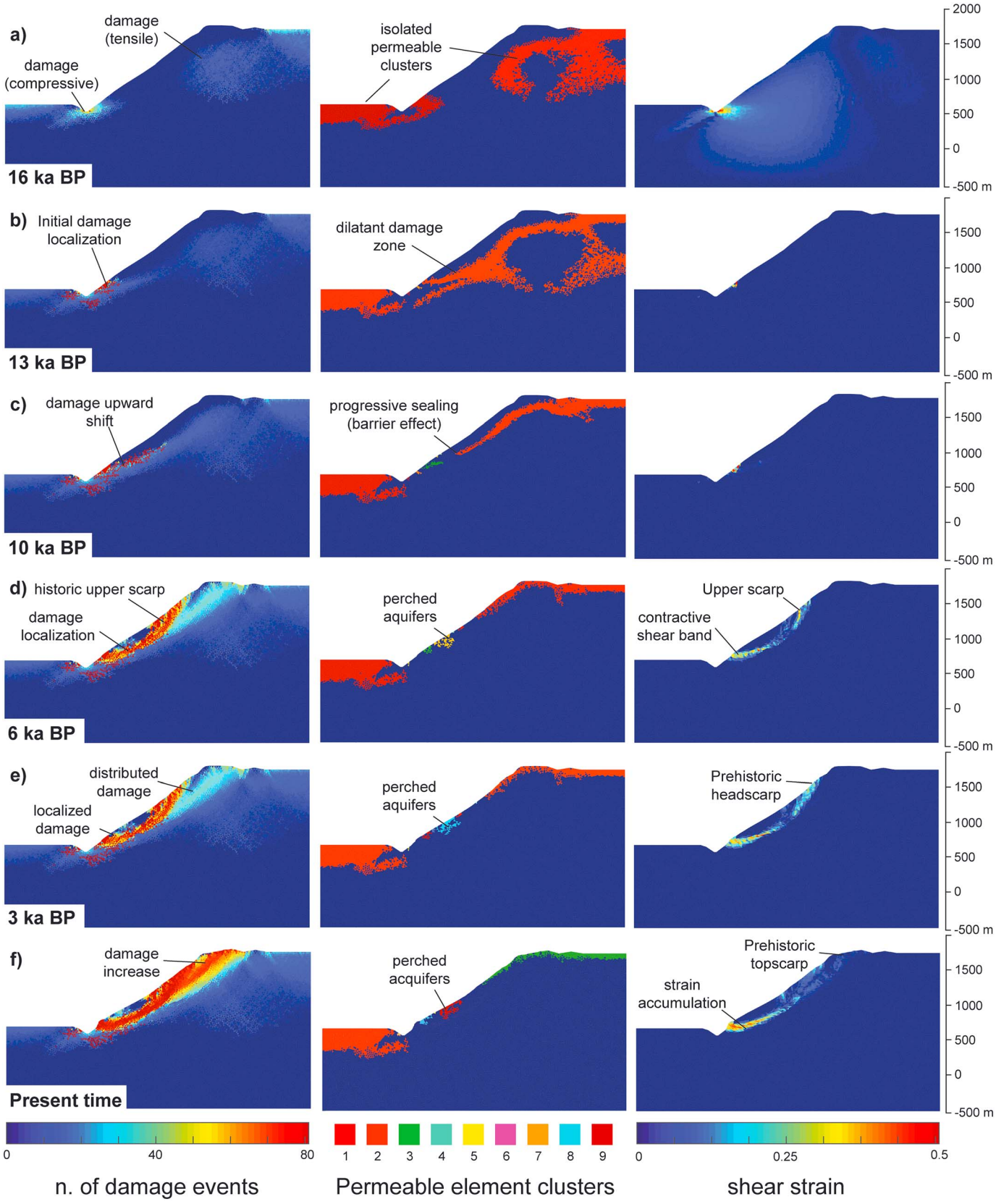

Figure 9. Model results at different times after LGM to present day, showing stages of progressive slope failure through the evolution of damage, permeable element clusters, and shear strain. Real time is scaled from model time based on available temporal constrains (see text for explanation).

outcomes of long-term slope evolution. The model predicts the occurrence of a compound rockslide suspended over the valley floor (Figure 8b). The rockslide overlies a zone of localized damage extending from the rockslide toe (about 700 m asl) to the top of the slope, where it diffusely emerges in the subdued slope sector above 1700 m asl corresponding to the upper "prehistoric top scarp." The simulated rockslide depth (100 to 180 m) is biased by the mesh size effect on the simulated basal shear zone thickness but consistent with the spatial pattern outlined by site investigations and with the observation of damaged material below the rockslide (Figures 8b and 8c). In any case, preliminary parametric analyses of mesh size effects had showed that predicted failure mechanisms remain consistent for mesh element sizes less than 50 m (i.e., 3% of model vertical size).

Vertical profiles of simulated horizontal displacement (Figure 8c), corresponding to model "virtual inclinometers," highlight relatively uniform displacements up to 100 m in depth (180 m upslope), gradually decreasing at further depth. Horizontal displacements emphasize the observed extent and compound kinematics of the rockslide, which is shallower than the damaged zone depth. The slope accumulated large vertical displacements in the upper part (upper scarp), whereas dominant horizontal displacements below 1100 m asl accounts for the historic lower scarp features.

The predicted spatial pattern of damage within the rockslide mass is consistent with borehole data, with generally more distributed damage close to the slope toe and above the lower scarp (Figures 8b and 8c). Below the lower scarp, damage is less intense within the rockslide mass but more localized in a basal shear zone (Figures 5 and 8c). Notably, in S113 good-quality remnant overlies intensely fractured rock mass, with damage extending up to 300 m below. The different degrees of damage and strain localization simulated along the basal shear zone mirrors some textural features of cataclastic breccias observed in boreholes (Figure 4), which are thicker and more comminuted in the lower part of the slope than in the upper. The model is also able to quantify the impact of damage on rock mass properties in different slope sectors, with simulated and observed GSI distributions in close agreement (Figure 8a). Starting from initial values in the range 75–85, progressive damage led to degradation of rock mass properties to values in the range 50–60 below the rockslide. Inside the rockslide, gravitational deformation contributed to further damage and lower GSI values, accounting for observed loss of structure and intense fracturing.

Damage mechanisms constrain the final distribution of permeable element clusters, and thus of water pressure distribution in the differentiated rockslide body. Here a fully interconnected (i.e., one cluster) perched aquifer occurs in the slope portion below the lower scarp, within the rockslide and in the damage zone just below (Cluster 5, Figure 8d). Additional smaller perched aquifers occur upslope, above the rockslide base and at slope crest. Results are consistent with site investigation data (Figures 5 and 8d) and with the strong sensitivity of the present-day rockslide to external hydrological inputs, especially in the lower part of the slope (Agliardi & Crosta, 2014).

4.2. Time-Dependent Evolution

The explicitly time-dependent nature of our model provides an opportunity to track the mechanisms of slope damage, water occurrence, deformation, and failure in an approximate real-time framework, obtained by scaling model time to available absolute constraints.

After complete deglaciation, initial damage nucleation occurs at 16 ka B.P. (i.e., 5 ka since the start of deglaciation) at slope toe (compression) and crest (extension) as a delayed response to valley debuttressing. This is associated to the onset of isolated permeable element clusters and negligible slope deformation (Figure 9a). Further on in the Lateglacial (13 ka B.P.; Figure 9b), initial damage localization starts above valley bottom (500 to 700 m asl) and progresses upward, resulting in the formation of an interconnected dilatant zone. This forms a connected aquifer layer and promotes further damage accumulation in an embryonal basal deformation zone, although no strain localization occurs at this stage.

During early Holocene (10 ka B.P.; Figure 9c) a major change occurs: damage accumulation shifts upward, shear strain localization initiates, and the previously dilatant damage zone evolves into a compacting shear zone, leading to the progressive hydraulic sealing of the upcoming rockslide basal shear zone. We interpret this stage as the rockslide nucleation stage. Complete rockslide differentiation is reached during middle Holocene (8–6 ka B.P., Figure 9d), when damage zones extending from slope toe to the scarps located around 1,400 m asl develop, suggesting that the prehistoric headscarp and top scarp formed at this stage. After shear

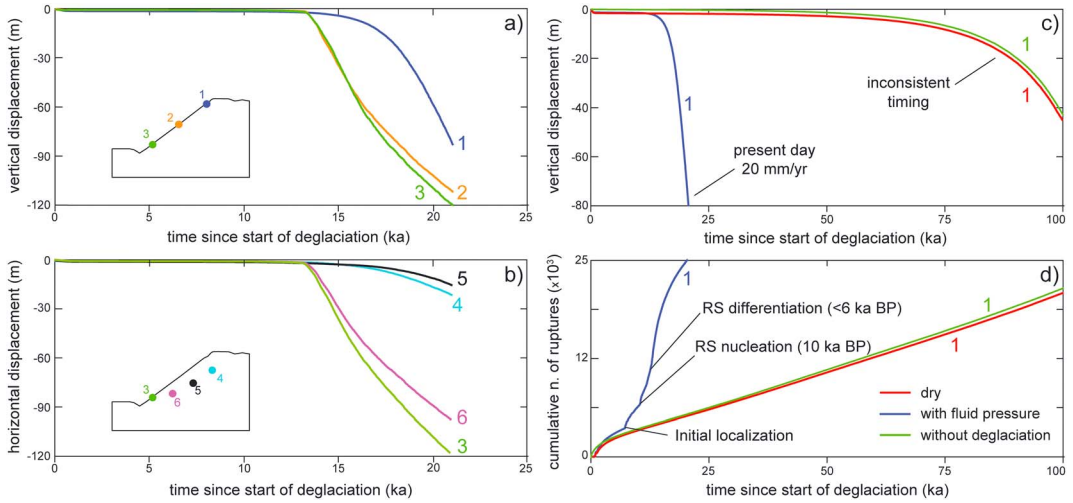

Figure 10. (a, b) Vertical and horizontal displacements versus time of selected observation points at key slope observation points (insets). (c) Long-term displacement-time curves (observation point 1) simulated accounting for deglaciation and water pressures (blue), deglaciation in dry conditions (red), and water pressures without deglaciation (green); (d) long-term damage evolution (cumulative numbers of ruptures, observation point 1), simulated accounting for deglaciation and water pressures (blue), deglaciation in dry conditions (red), and water pressures without deglaciation (green).

zone contraction and complete sealing, partially connected permeable element clusters form within the rockslide body. The associated increase of rockslide sensitivity to hydrological inputs is mirrored by an order-of-magnitude increase of displacement rate (Figures 10a and 10b). This is the stage of rockslide differentiation.

During the next 6 ka until present day, progressive slope failure continues, with the upslope retrogression of the basal shear zone to the prehistoric headscarp (Figure 9e), and the eventual formation of the subdued "prehistoric" top scarp area upslope. This evolution is associated with further nonlinear increase of displacement rates up to 20 mm/a (Figure 10c), consistent with present-day measured values. Vertical displacement at the rockslide headscarp reaches 80 m, and the present-day perched aquifer reaches complete development.

We tracked simulated displacements at several observation points, located along the slope and the rockslide shear zone, in order to better constrain the temporal evolution of different slope sectors. The prehistoric headscarp exhibits contemporary activation (6 ka B.P.) but smaller vertical displacements with respect to the upper scarp and rockslide toe (Figure 10a). Horizontal displacements tracked along the basal shear zone suggest activation of lower sector around 8 ka B.P. followed after few thousands year by the contemporary activation of middle and upper portions (Figure 10b).

4.3. Long-Term Effects of Water Pressure and Deglaciation

The model results discussed above suggest a key role of both water pressure distributions and deglaciation in the long-term evolution of the slope. In order to elucidate this role, we ran additional models with the same characteristics of the one presented above (Figures 11a–11c) but (a) with deglaciation in dry conditions (Figures 11d–11f) and (b) allowing water pressure distributions without deglaciation (Figures 11g–11i). Simulating dry conditions results in inconsistent global slope failure geometries and mechanisms, with deep rotational kinematics and excessive damage localization. Simulations with and without water pressure are also characterized by a sharply different lifetime, as the "dry" model takes an excessively long time ($>$100 ka) to reach observed displacement (Figure 10c). The simulation neglecting deglaciation, that is, on a glacier-free slope, provides result very similar to the dry model in terms of both damage (Figure 11g) and total displacement (Figures 11h and 11i). Despite the simplified initial conditions, this suggests that deglaciation not only causes slope debuttressing but induces in the slope the amount of mechanical damage required to start the hydromechanically coupled processes driving progressive failure to the observed outcome. In this perspective, the Spriana rockslide can be properly be defined as "paraglacial."

Accounting for water occurrence and deglaciation affects the long-term damage evolution in the slope, here represented in terms of cumulative number of ruptures versus time (Figure 10d). In fact, the model with water pressure results in a fluctuating trend, resulting from the superposition of long-term hydromechanical pulses

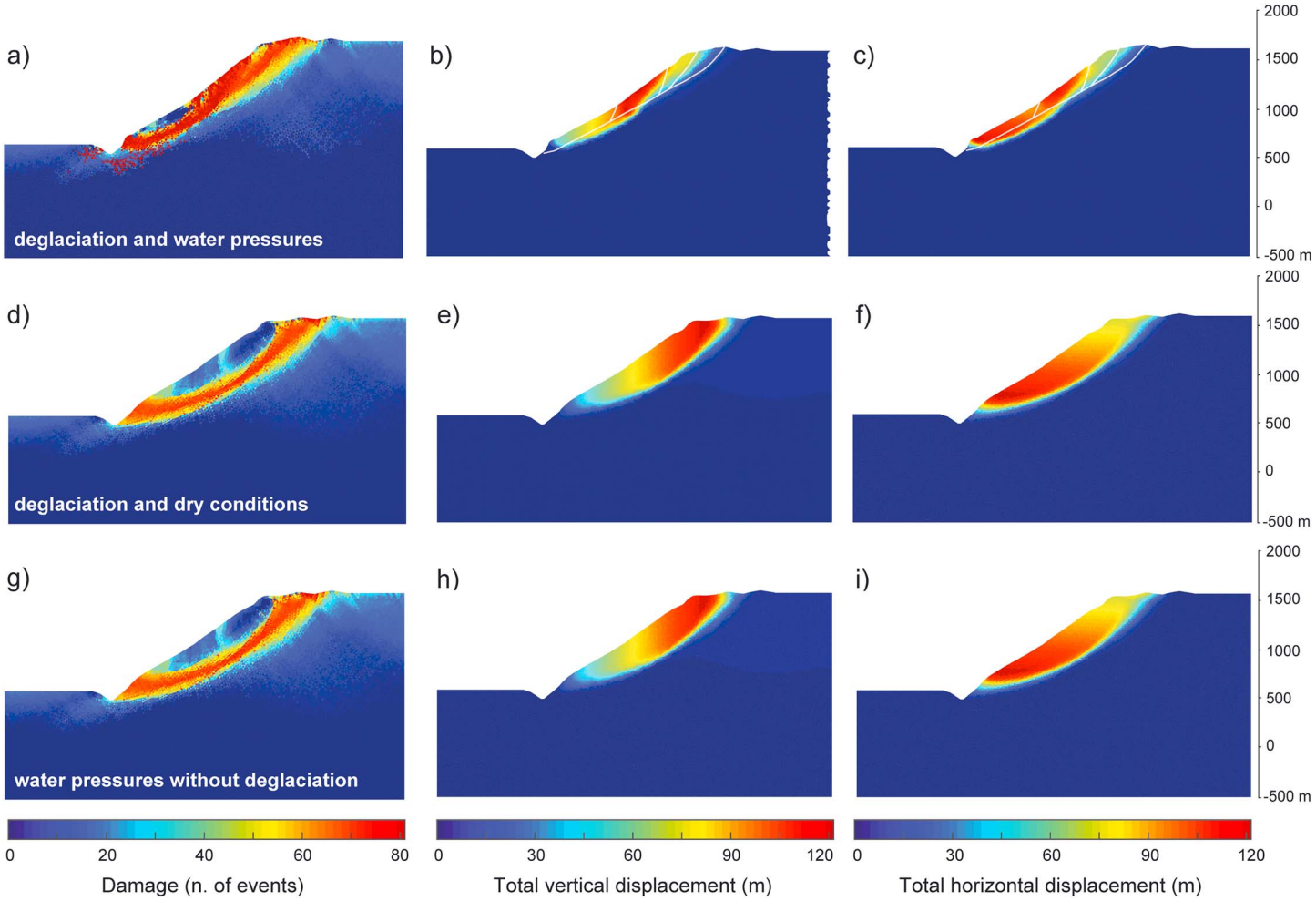

Figure 11. Comparison between simulated (a, d, and g) damage patterns, (b, e, and h) vertical displacements, and (c, f, and i) horizontal displacements for models accounting for deglaciation and water pressures, deglaciation in dry conditions, and water pressures without deglaciation, respectively (see text for explanation).

(associated to major damage evolution stages) over a long-term material creep component. This trend is not reproduced by the dry and ice-free models, which show a decelerating creep followed by a long period of nearly steady state creep, which develops over a much longer time interval than in wet conditions.

Finally, we investigated the ability of our model to simulate the hydromechanical behaviour of rockslides after their mechanical differentiation. We ran different models with progressively higher values of w (degree of permeable element cluster filling). We kept permeable cluster filling constant to $w = 0.35$ until 5,000 years B.P. (i.e., after rockslide differentiation); then we increased w to 0.50, 0.75, or 1 until the end of the model. Results clearly show that, if water pressures are changed after the complete mechanical differentiation of the rockslide, they do not affect the rockslide mechanisms and damage patterns anymore, but have strong impacts on rockslide creep rates and times to failure (Figure 12). Increasing w results in a slope lifetime shortening, especially for $w > 0.5$, for which slope life cycle shortening up to 2,000 years (10% of total slope lifetime) is observed. At the same time, increasing water pressure results in abrupt increases of rockslide displacement rates. These results suggest that "mature" rockslides become hydromechanically independent from the rest of the slope and increasingly more sensitive to hydrological triggers (Agliardi & Crosta, 2014; Crosta et al., 2014; Preisig et al., 2015).

4.4. Long-Term Evolution of Alpine Rock Slopes

Our results allow to draw some important considerations: (1) the paraglacial period of adjustment for alpine slopes in hard rock may be much longer then postulated by most authors and can be ideally extended up to slope collapse or reaching of ultimate stability conditions (Ballantyne et al., 2014; Cruden & Hu, 1993; Le Roux

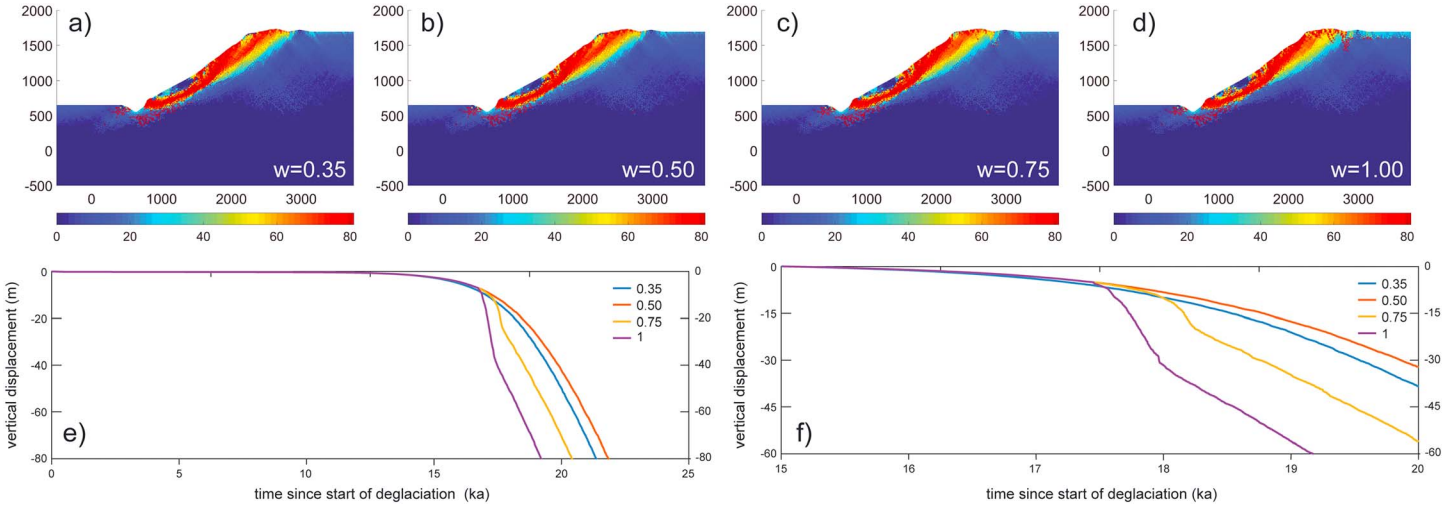

Figure 12. Damage patterns at the end of simulations performed with the following: (a) constant $w = 0.35$ for the entire duration of simulation; (b) $w = 0.35$ until 5 ka B.P. followed by increase to 0.50, (c) $w = 0.35$ until 5 ka B.P. followed by increase to 0.75 and, (d) $w = 0.35$ until 5 ka B.P. followed by increase to 1. Global (e) trends and (f) details of vertical displacement-time curves (observation point 1 of Figure 10) show increasing displacement rates and slope lifetime shortening with increasing w, while damage patterns and failure mechanisms are not affected after rockslide differentiation.

et al., 2009; Figures 10 and 11); (2) the initiation of debuttressing-induced damage and its localization are prerequisites for water circulation in hydraulically interconnected slope sectors, strain localization, and slope deformation. Thus, the onset of large slope instability occurs in discrete evolutionary stages (Figure 10); (3) in this framework, evolutionary stages can affect different slope sectors at different time, with delays up to some thousands of years (Figure 11); (4) rockslide differentiation by complete development of contractive (sealing) cataclastic shear zones, and the associated increase of hydromechanical coupling and sensitivity to external triggers, is the very last evolutionary stage.

The above considerations allow us to contribute to a more general discussion on the timing and controls of large alpine rock slope instabilities, in the framework of postglacial evolution of Alpine landscapes. Two different temporal clusters of rock slope instability events (including both initiation/reactivation and catastrophic collapse) have been documented in the literature using absolute dating techniques (Le Roux et al., 2009; Prager et al., 2008; Zerathe et al., 2014, and references therein). The first cluster, between 11 and 8 ka B.P., has been suggested as possibly related to paraglacial readjustment, by progressive failure at the transition with the Holocene (Prager et al., 2008). The second, concerning the period 5–3 ka B.P., was mainly suggested to be related to seismicity (Prager et al., 2008) and/or paleohydrologic pulses during Middle-Holocene climatic transition (Prager et al., 2008; Zerathe et al., 2014). Interestingly, ages of both clusters roughly correspond to two major evolutionary steps predicted by our models, namely, (a) rockslide nucleation (10 ka B.P.) and (b) rockslide differentiation (6 ka B.P.). We suggest, and submit to further testing, the hypothesis that progressive failure processes in subcritical stress conditions may have contributed to both age clusters in a unique postdeglaciation evolutionary framework, with different outcomes (slow deformations or catastrophic collapse) depending on site-specific topographic, lithological, and structural features. In this view, particular assumptions on paleohydrologic conditions may not be required to explain Mid-Holocene rockslide clustering, although wet periods would have positively contributed to rockslide differentiation.

5. Conclusions

We implemented a damage-based, time-dependent modeling approach to reproduce the entire life cycle of a large alpine rock slope, starting from the Last Glacial Maximum to the present time. The application of continuum damage mechanics to real, large rock slope instabilities provided the opportunity to investigate the mechanisms and timing of long-term evolution from deglaciation to modern conditions.

The model is able to reproduce both localized and diffuse patterns of brittle damage, depending on the combination of material properties and water pressure distribution. Deglaciation and related damage-dependent

fluid pressure distributions strongly affect the geometry and the timing of instability, resulting in the commonly observed interplay between creep (up to tertiary regime) and hydrological forcing, which becomes more and more important throughout slope evolution. As an emerging property, the model simulates a contractive behavior of rockslide shear zones, accounting for the hydraulic barrier effect leading to the development of perched aquifers and the "differentiation" of rockslides characterized by a high sensitivity to external triggers.

The model is able to link rockslide evidence and processes, commonly observed in real slopes, in the framework of a continuous mechanical history, unfolding since the post-LGM. Models simulate deglaciation-induced mechanical perturbations lasting for several thousands of years, suggesting a long duration of the paraglacial period in large rock slopes. The development of large slope instabilities is conditioned by discrete steps related to damage and subsequent development of strain localization and rockslide differentiation. The simulated timing of these steps is consistent with available dating constraints, suggesting a major role of long-term progressive damage in the development of Holocene rockslides and present-day geohazards.

Acknowledgments

Data used for this paper are properly cited and referred to in the main text and reference list. Data output is included in the tables, figures, and supporting information. Raw data are available from F. A. (e-mail: federico.agliardi@unimib.it). The authors are grateful to L. Dei Cas and G. Mannucci (ARPA Lombardia) for access to drill cores. We thank R. Scotti for the fruitful discussions on the glacial and postglacial evolution of Valtellina. K. Leith and an anonymous reviewer greatly contributed to improve the paper. The work was partially supported by project "Slow2Fast - Long-term activity, damage and collapse potential of large slow-moving landslides in rock in Lombardia" funded by Fondazione Cariplo, grant 2016-0757. The authors declare no conflicts of interest.

References

Agliardi, F., & Crosta, G. B. (2014). Long and short-term controls on the Spriana rockslide (Central Alps, Italy). In *Landslide science for a safer geoenvironment* (pp. 243–249). Springer International Publishing. https://doi.org/10.1007/978-3-319-05050-8_37

Agliardi, F., Crosta, G. B., & Frattini, P. (2012). Slow rock slope deformation. In J. J. Clague & D. Stead (Eds.), *Landslides: Types, mechanisms and modeling* (pp. 207–221). Cambridge: Cambridge University Press.

Agliardi, F., Crosta, G. B., Frattini, P., & Malusà, M. G. (2013). Giant non-catastrophic landslides and the long-term exhumation of the European Alps. *Earth and Planetary Science Letters*, *365*, 263–274. https://doi.org/10.1016/j.epsl.2013.01.030

Agliardi, F., Crosta, G., & Zanchi, A. (2001). Structural constraints on deep-seated slope deformation kinematics. *Engineering Geology*, *59*(1-2), 83–102. https://doi.org/10.1016/S0013-7952(00)00066-1

Agliardi, F., Crosta, G. B., Zanchi, A., & Ravazzi, C. (2009). Onset and timing of deepseated gravitational slope deformations in the eastern Alps, Italy. *Geomorphology*, *103*, 113–129. https://doi.org/10.1016/j.geomorph.2007.09.015

Agliardi, F., Dobbs, M. R., Zanchetta, S., & Vinciguerra, S. (2017). Folded fabric tunes rock deformation and failure mode in the upper crust. *Scientific Reports*, *7*(1), 15290. https://doi.org/10.1038/s41598-017-15523-1

Agliardi, F., Sapigni, M., & Crosta, G. B. (2016). Rock mass characterization by high-resolution sonic and GSI borehole logging. *Rock Mechanics and Rock Engineering*, *49*(11), 4303–4318. https://doi.org/10.1007/s00603-016-1025-x

Agliardi, F., Zanchetta, S., & Crosta, G. B. (2014). Fabric controls on the brittle failure of folded gneiss and schist. *Tectonophysics*, *637*, 150–162. https://doi.org/10.1016/j.tecto.2014.10.006

Ambrosi, C., & Crosta, G. B. (2006). Large sackung along major tectonic features in the Central Italian Alps. *Engineering Geology*, *83*, 183–200. https://doi.org/10.1016/j.enggeo.2005.06.031

Amitrano, D., Grasso, J. R., & Hantz, D. (1999). From diffuse to localised damage through elastic interaction. *Geophysical Research Letters*, *26*, 2109–2112. https://doi.org/10.1029/1999GL900388

Amitrano, D., & Helmstetter, A. (2006). Brittle creep, damage, and time to failure in rocks. *Journal of Geophysical Research*, *111*, B11201. https://doi.org/10.1029/2005JB004252

Atkinson, B. K. (1984). Subcritical crack growth in geological materials. *Journal of Geophysical Research*, *89*, 4077–4114. https://doi.org/10.1029/JB089iB06p04077

Augustinus, P. C. (1995). Glacial valley cross-profile development: The influence of in situ rock stress and rock mass strength, with examples from the Southern Alps, New Zealand. *Geomorphology*, *14*(2), 87–97. https://doi.org/10.1016/0169-555X(95)00050-X

Ballantyne, C. K. (2002). Paraglacial geomorphology. *Quaternary Science Reviews*, *21*, 1935–2017. https://doi.org/10.1016/S0277-3791(02)00005-7

Ballantyne, C. K., Sandeman, G. F., Stone, J. O., & Wilson, P. (2014). Rock-slope failure following Late Pleistocene deglaciation on tectonically stable mountainous terrain. *Quaternary Science Reviews*, *86*, 144–157. https://doi.org/10.1016/j.quascirev.2013.12.021

Barton, N. (2007). *Rock quality, seismic velocity, attenuation and anisotropy*, (p. 450). London: Taylor and Francis.

Belloni, L., & Gandolfo, M. (1997). La frana di Spriana. *Geologia tecnica ed ambientale*, *3*, 7–36.

Bini, A., Buoncristiani, J.-F., Couterrand, S., Ellwanger, D., Felber, M., Florineth, D., … Schoeneich, P. (2009). *La Svizzera Durante L'ultimo Massimo Dell'epoca Glaciale, 1:500 000*. Swisstopo, Wabern, Switzerland.

Brideau, M. A., Yan, M., & Stead, D. (2009). The role of tectonic damage and brittle rock fracture in the development of large rock slope failures. *Geomorphology*, *103*(1), 30–49. https://doi.org/10.1016/j.geomorph.2008.04.010

Brocklehurst, S. H., & Whipple, K. X. (2004). Hypsometry of glaciated landscapes. *Earth Surface Processes and Landforms*, *29*(7), 907–926. https://doi.org/10.1002/esp.1083

Cappa, F., Guglielmi, Y., Soukatchoff, V. M., Mudry, J., Bertrand, C., & Charmoille, A. (2004). Hydromechanical modeling of a large moving rock slope inferred from slope levelling coupled to spring long-term hydrochemical monitoring: Example of the La Clapiere landslide (Southern Alps, France). *Journal of Hydrology*, *291*, 67–90. https://doi.org/10.1016/j.jhydrol.2003.12.013

Chigira, M. (1992). Long-term gravitational deformation of rocks by mass rock creep. *Engineering Geology*, *32*(3), 157–184. https://doi.org/10.1016/0013-7952(92)90043-X

Church, M., & Ryder, J. M. (1972). Paraglacial sedimentation: A consideration of fluvial processes conditioned by glaciation. *Geological Society of America Bulletin*, *83*(10), 3059–3072. https://doi.org/10.1130/0016-7606(1972)83

Clark, P. U., Dyke, A. S., Shakun, J. D., Carlson, A. E., Clark, J., Wohlfarth, B., … McCabe, A. M. (2009). The last glacial maximum. *Science*, *325*, 710–714. https://doi.org/10.1126/science.1172873

Corominas, J., Moya, J., Ledesma, A., Lloret, A., & Gili, J. A. (2005). Prediction of ground displacements and velocities from groundwater level changes at the Vallcebre landslide (Eastern Pyrenees, Spain). *Landslides*, *2*(2), 83–96.

Cossart, E., Braucher, R., Fort, M., Bourlès, D. L., & Carcaillet, J. (2008). Slope instability in relation to glacial debuttressing in alpine areas (Upper Durance catchment, southeastern France): Evidence from field data and 10 Be cosmic ray exposure ages. *Geomorphology*, *95*, 3–26. https://doi.org/10.1016/j.geomorph.2006.12.022

Crosta, G. (1996). Landslide, spreading, deep seated gravitational deformation: Analysis, examples, problems and proposals. *Geografia Fisica e Dinamica Quaternaria*, *19*(2), 297–313.

Crosta, G. B., & Agliardi, F. (2003). Failure forecast for large rock slides by surface displacement measurements. *Canadian Geotechnical Journal*, *40*(1), 176–191. https://doi.org/10.1139/t02-085

Crosta, G. B., di Prisco, C., Frattini, P., Frigerio, G., Castellanza, R., & Agliardi, F. (2014). Chasing a complete understanding of the triggering mechanisms of a large rapidly evolving rockslide. *Landslides*, *11*(5), 747–764. https://doi.org/10.1007/s10346-013-0433-1

Crosta, G. B., Frattini, P., & Agliardi, F. (2013). Deep seated gravitational slope deformations in the European Alps. *Tectonophysics*, *605*, 13–33. https://doi.org/10.1016/j.tecto.2013.04.028

Cruden, D. M., & Hu, X. Q. (1993). Exhaustion and steady state models for predicting landslide hazards in the Canadian Rocky Mountains. *Geomorphology*, *8*(4), 279–285. https://doi.org/10.1016/0169-555X(93)90024-V

De Caro, M., Crosta, G. B., Castellanza, R., Agliardi, F., Volpi, G., & Alberti, S. (2016). 2D modelling of rockslide displacements by non-linear time dependent relationships. In landslides and engineered slopes. Experience, theory and practice. Proceedings of the 12th international symposium on landslides (Napoli, Italy, 12-19 June 2016). https://doi.org/10.1201/b21520-89

Deline, P., Gruber, S., Delaloye, R., Fischer, L., Geertsema, M., Giardino, M., … Schoeneich, P. (2015). Ice loss and slope stability in high-mountain regions. In W. Haeberli, C. Whiteman, & J. F. Shroder (Eds.), *Snow and ice-related hazards, risks, and disasters*, (pp. 521–561). Saint Louis: Elsevier science. https://doi.org/10.1016/B978-0-12-394849-6.00015-9

Dershowitz, W. S., & Herda, H. H. (1992). Interpretation of fracture spacing and intensity. In the 33th US Symposium on Rock Mechanics (USRMS). American Rock Mechanics Association.

Dortch, J. M., Owen, L. A., Haneberg, W. C., Caffee, M. W., Dietsch, C., & Kamp, U. (2009). Nature and timing of large landslides in the Himalaya and Transhimalaya of northern India. *Quaternary Science Reviews*, *28*, 1037–1054. https://doi.org/10.1016/j.quascirev.2008.05.002

Eberhardt, E., Stead, D., & Coggan, J. S. (2004). Numerical analysis of initiation and progressive failure in natural rock slopes—The 1991 Randa rockslide. *International Journal of Rock Mechanics and Mining Sciences*, *41*, 69–87. https://doi.org/10.1016/S1365-1609(03)00076-5

Eberhardt, E., Stead, D., & Stimpson, B. (1999). Quantifying progressive pre-peak brittle fracture damage in rock during uniaxial compression. *International Journal of Rock Mechanics and Mining Sciences*, *36*(3), 361–380. https://doi.org/10.1016/S0148-9062(99)00019-4

Einstein, H. H., Veneziano, D., Baecher, G. B., & O'Reilly, K. J. (1983). The effect of discontinuity persistence on rock slope stability. *International Journal of Rock Mechanics and Mining Science and Geomechanics Abstracts*, *20*(5), 227–236. https://doi.org/10.1016/0148-9062(83)90003-7

El Bedoui, S., Guglielmi, Y., Lebourg, T., & Perez, J.-L. (2009). Deep seated failure propagation in a fractured rock slope over 10,000 years: The la Clapiere slope, the south-eastern French Alps. *Geomorphology*, *105*, 232–238. https://doi.org/10.1016/j.geomorph.2008.09.025

Emery, J. J. (1979). Simulation of slope creep. In B. Voight (Ed.), *Rock slides and avalanches, developments in geotechnical engineering* (Vol. 14b, pp. 669–691). Amsterdam: Elsevier.

Fortin, J., Stanchits, S., Vinciguerra, S., & Guéguen, Y. (2011). Influence of thermal and mechanical cracks on permeability and elastic wave velocities in a basalt from Mt. Etna volcano subjected to elevated pressure. *Tectonophysics*, *503*, 60–74. https://doi.org/10.1016/j.tecto.2010.09.028

Gercek, H. (2007). Poisson's ratio values for rocks. *International Journal of Rock Mechanics and Mining Sciences*, *44*, 1–13. https://doi.org/10.1016/j.ijrmms.2006.04.011

Guglielmi, Y., Cappa, F., & Binet, S. (2005). Coupling between hydrogeology and deformation of mountainous rock slopes: Insights from La Clapière area (southern Ips, France). *Comptes Rendus Geoscience*, *337*, 1154–1163. https://doi.org/10.1016/j.crte.2005.04.016

Hajiabdolmajid, V., Kaiser, P. K., & Martin, C. D. (2002). Modelling brittle failure of rock. *International Journal of Rock Mechanics and Mining Sciences*, *39*(6), 731–741. https://doi.org/10.1016/S1365-1609(02)00051-5

Harbor, J. M. (1992). Numerical modeling of the development of U-shaped valleys by glacial erosion. *Geological Society of America Bulletin*, *104*(10), 1364–1375. https://doi.org/10.1130/0016-7606(1992)104

Heap, M. J., Baud, P., Meredith, P. G., Bell, A. F., & Main, I. G. (2009). Time-dependent brittle creep in Darley Dale sandstone. *Journal of Geophysical Research*, *114*, B07203. https://doi.org/10.1029/2008JB006212

Helmstetter, A., & Garambois, S. (2010). Seismic monitoring of Séchilienne rockslide (French Alps): Analysis of seismic signals and their correlation with rainfalls. *Journal of Geophysical Research*, *115*, F03016. https://doi.org/10.1029/2009JF001532

Hoek, E., & Brown, E. T. (1980). Underground excavations in rock (no. monograph). ISBN: 0900488557

Hoek, E., Carranza-Torres, C., & Corkum, B. (2002). Hoek-Brown failure criterion—2002 edition. Proceedings north American rock mechanics society. Toronto, July 2002.

Hoek, E., & Diederichs, M. S. (2006). Empirical estimation of rock mass modulus. *International Journal of Rock Mechanics and Mining Sciences*, *43*, 203–215. https://doi.org/10.1016/j.ijrmms.2005.06.005

Hoek, E., Kaiser, P. K., & Bawden, W. (1995). Support of underground excavations in hard rock. ISBN 9789054101864

Holm, K., Bovis, M. J., & Jakob, M. (2004). The landslide response of alpine basins to post-Little Ice Age glacial thinning and retreat in southwestern British Columbia. *Geomorphology*, *57*, 201–216. https://doi.org/10.1016/S0169-555X(03)00103-X

Ivy-Ochs, S., Kerschner, H., Kubik, P. W., & Schlüchter, C. (2006). Glacier response in the European Alps to Heinrich Event 1 cooling: The Gschnitz stadial. *Journal of Quaternary Science*, *21*, 115–130. https://doi.org/10.1002/jqs.955

Ivy-Ochs, S., Kerschner, H., Reuther, A., Preusser, F., Heine, K., Maisch, M., … Schlüchter, C. (2008). Chronology of the last glacial cycle in the European Alps. *Journal of Quaternary Science*, *23*, 559–573. https://doi.org/10.1002/jqs.1202

Kachanov, L. (1986). *Introduction to continuum damage mechanics* (Vol. 10). Brookline, MA: Springer science and business media.

Katz, O., & Reches, Z. E. (2004). Microfracturing, damage, and failure of brittle granites. *Journal of Geophysical Research*, *109*, B01206. https://doi.org/10.1029/2002JB001961

Korup, O., Densmore, A. L., & Schlunegger, F. (2010). The role of landslides in mountain range evolution. *Geomorphology*, *120*, 77–90. https://doi.org/10.1016/j.geomorph.2009.09.017

Lacroix, P., & Amitrano, D. (2013). Long-term dynamics of rockslides and damage propagation inferred from mechanical modeling. *Journal of Geophysical Research: Earth Surface*, *118*, 2292–2307. https://doi.org/10.1002/2013JF002766

Leith, K., Moore, J. R., Amann, F., & Loew, S. (2014). In situ stress control on micro-crack generation and macroscopic extensional fracture in exhuming bedrock. *Journal of Geophysical Research: Solid Earth*, *119*, 594–615. https://doi.org/10.1002/2012JB009801

Le Roux, O., Schwartz, S., Gamond, J. F., Jongmans, D., Bourles, D., Braucher, R., & Leanni, L. (2009). CRE dating on the head scarp of a major landslide (Séchilienne, French Alps), age constraints on Holocene kinematics. *Earth and Planetary Science Letters*, *280*, 236–245. https://doi.org/10.1016/j.epsl.2009.01.034

Marinos, P., & Hoek, E. (2000). GSI: A geologically friendly tool for rock mass strength estimation. In ISRM International Symposium. International Society for Rock Mechanics.

Martin, C. D., & Chandler, N. A. (1994). The progressive fracture of lac du bonnet granite. *International Journal of Rock Mechanics and Mining Science and Geomechanics Abstracts*, *31*(6), 643–659. https://doi.org/10.1016/0148-9062(94)90005-1

McColl, S. T. (2012). Paraglacial rock-slope stability. *Geomorphology*, *153-154*, 1–16. https://doi.org/10.1016/j.geomorph.2012.02.015

Miller, D. J., & Dunne, T. (1996). Topographic perturbations of regional stresses and consequent bedrock fracturing. *Journal of Geophysical Research*, *101*, 25,523–25,536. https://doi.org/10.1029/96JB02531

Molnar, P. (2004). Late Cenozoic increase in accumulation rates of terrestrial sediment: How might climate change have affected erosion rates? *Annual Review of Earth and Planetary Sciences*, *32*(1), 67–89. https://doi.org/10.1146/annurev.earth.32.091003.143456

Palmstrom, A. (2005). Measurements of and correlations between block size and rock quality designation (RQD). *Tunnelling and Underground Space Technology*, *20*, 362–377. https://doi.org/10.1016/j.tust.2005.01.005

Pariseau, W. G., & Voight, B. (1979). Rockslides and avalanches: Basic principles and perspectives in the realm of civil and mining operations. *Rockslides and Avalanches*, *2*, 1–92, ISBN: 9780444598011

Prager, C., Zangerl, C., Patzelt, G., & Brandner, R. (2008). Age distribution of fossil landslides in the Tyrol (Austria) and its surrounding areas. *Natural Hazards and Earth System Sciences*, *8*, 377–407. https://doi.org/10.5194/nhess-8-377-2008

Preisig, G., Eberhardt, E., Smithyman, M., Preh, A., & Bonzanigo, L. (2015). Hydromechanical rock mass fatigue in deep-seated landslides accompanying seasonal variations in pore pressures. *Rock Mechanics and Rock Engineering*, 1–19. https://doi.org/10.1007/s00603-016-0912-5

Riva F. (2017). Damage-based long-term modelling of paraglacial to postglacial evolution of alpine rock slopes. PhD thesis, University of Milano-Bicocca.

Riva F., Agliardi, F., Amitrano, D., & Crosta, G. B. (2016). Damage-based long term modelling of a large alpine rock slope. In landslides and engineered slopes. Experience, theory and practice. Proceedings of the 12th international symposium on landslides (Napoli, Italy, 12–19 June 2016). https://doi.org/10.1201/b21520-214

Rose, N. D., & Hungr, O. (2007). Forecasting potential rock slope failure in open pit mines using the inverse-velocity method. *International Journal of Rock Mechanics and Mining Sciences*, *44*, 308–320. https://doi.org/10.1016/j.ijrmms.2006.07.014

Rutqvist, J. (2015). Fractured rock stress-permeability relationships from in situ data and effects of temperature and chemical-mechanical couplings. *Geofluids*, *15*(1-2), 48–66. https://doi.org/10.1111/gfl.12089

Rutqvist, J., & Stephansson, O. (2003). The role of hydromechanical coupling in fractured rock engineering. *Hydrogeology Journal*, *11*(1), 7–40. https://doi.org/10.1007/s10040-002-0241-5

Saito, M., & Uezawa, H. (1961). Failure of soil due to creep. In *Fifth international conference of soil mechanics and foundation engineering* (pp. 315–318). Dunod, Paris.

Savage, W. Z., Swolfs, H. S., & Powers, P. S. (1985). Gravitational stresses in long symmetric ridges and valleys. *International Journal of Rock Mechanics and Mining Science and Geomechanics Abstracts*, *22*(5), 291–302. https://doi.org/10.1016/0148-9062(85)92061-3

Sternai, P., Herman, F., Fox, M. R., & Castelltort, S. (2011). Hypsometric analysis to identify spatially variable glacial erosion. *Journal of Geophysical Research*, *116*, F03001. https://doi.org/10.1029/2010JF001823

Trommsdorf, V., Montrasio, A., Hermann, J., Müntenerl, O., Spillmann, P., & Gierè, R. (2005). The geological map of Val Malenco. *Schweizerische Mineralogische und Petrographische Mitteilungen*, *85*, 1–13.

Vallet, A., Charlier, J. B., Fabbri, O., Bertrand, C., Carry, N., & Mudry, J. (2015). Functioning and precipitation-displacement modelling of rainfall-induced deep-seated landslides subject to creep deformation. *Landslides*, 1–18. https://doi.org/10.1007/s10346-015-0592-3

Voight, B. (1989). A relation to describe rate-dependent material failure. *Science*, *243*(4888), 200–203.

Wirsig, C., Zasadni, J., Christl, M., Akçar, N., & Ivy-Ochs, S. (2016). Dating the onset of LGM ice surface lowering in the High Alps. *Quaternary Science Reviews*, *143*, 37–50. https://doi.org/10.1016/j.quascirev.2016.05.001

Zangerl, C., Eberhardt, E., & Perzlmaier, S. (2010). Kinematic behaviour and velocity characteristics of a complex deep-seated crystalline rockslide system in relation to its interaction with a dam reservoir. *Engineering Geology*, *112*, 53–67. https://doi.org/10.1016/j.enggeo.2010.01.001

Zavodni, Z. M., & Broadbent C. D. (1978). Slope failure kinematics. 19th US symposium on rock mechanics (USRMS). American rock mechanics association, 1978.

Zerathe, S., Lebourg, T., Braucher, R., & Bourlès, D. (2014). Mid-Holocene cluster of large-scale landslides revealed in the Southwestern Alps by 36 Cl dating. Insight on an Alpine-scale landslide activity. *Quaternary Science Reviews*, *90*, 106–127. https://doi.org/10.1016/j.quascirev.2014.02.015

Zoback, M. D., & Byerlee, J. D. (1975). The effect of cyclic differential stress on dilatancy in Westerly granite under uniaxial and triaxial conditions. *Journal of Geophysical Research*, *80*, 1526–1530. https://doi.org/10.1029/JB080i011p01526